Supporting Information

MXene Derived-TiO_2/β-Ag_2MoO_4 Nanocomposite: A Multifunctional Electrode for Enhanced Energy Storage in Supercapacitors and Lithium-Ion Batteries

Neha D. Panchal and Helen Annal Therese*

Futuristic Energy Storage Technology Lab (FESTL), Department of Chemistry, SRM Institute of Science and Technology, Kattankulathur, Chennai, 603 203, India

*Corresponding author e-mail: helena@srmist.edu.in

2.5. Physical Characterization

XRD studies were conducted using Cu Kα radiation (λ = 1.5406 Å, 40 kV, 40 mA) in the 2θ range of 5-90°. Raman analysis was done by Micro-Raman Spectrometer (LabRAM HR Evolution HORIBA France), using powder samples on a glass substrate. An Oxxius laser of 633 nm wavelength (having a max. power of 100 mW) was used throughout the complete measurement. The morphology and the elemental mapping of the heterostructure were analyzed using high-resolution scanning electron microscopy (HRSEM), Thermo Scientific Apreo instrument operated at an acceleration voltage of 20 kV. Transmission electron microscopy (TEM) images were collected using JEOL Japan, JEM-2100 plus transmission electron microscope operated at an acceleration voltage of 200 kV with the electron source of thermionic LaB_6 single crystal. X-ray photoelectron spectroscopic (XPS) measurements were done with PHI Versaprobe III XPS instrument, and all individual spectra were deconvoluted and fitted using the Shirley-type background function.

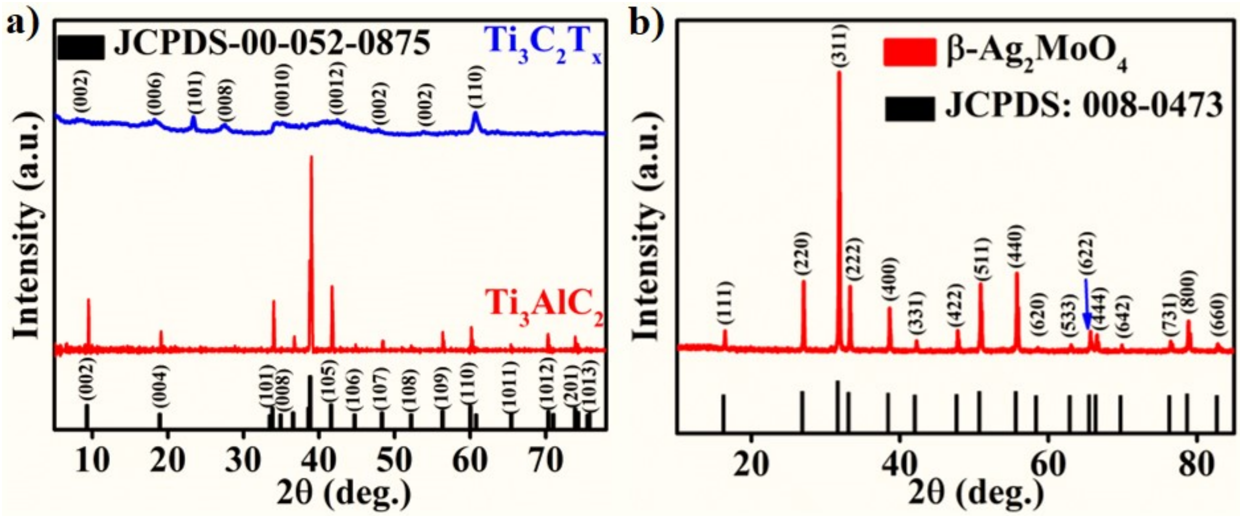

Figure S1. XRD pattern of (a) Ti_3AlC_2, $Ti_3C_2T_x$ and; (b) β-Ag_2MoO_4.

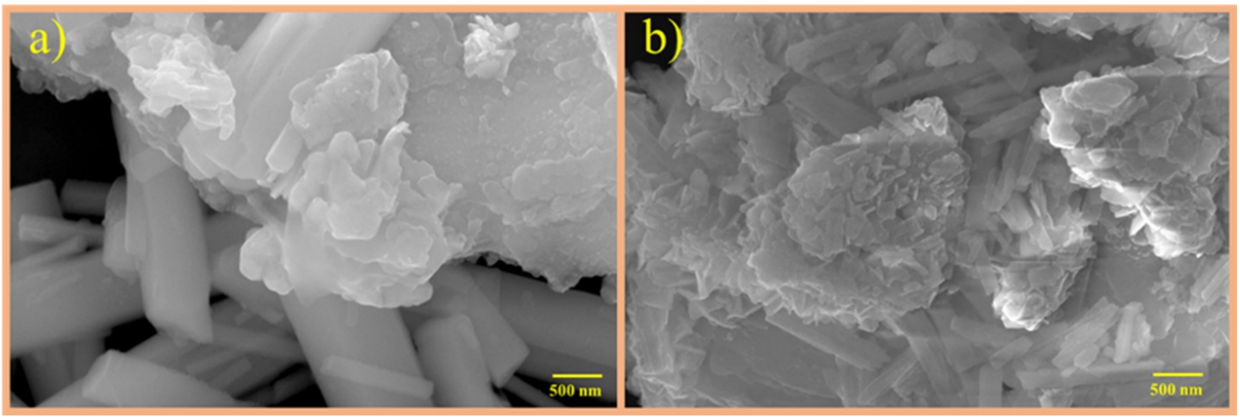

Figure S2. SEM image of (a) M-TiO_2/β-Ag_2MoO_4-1 and; (b) M-TiO_2/β-Ag_2MoO_4-3 nanocomposite.

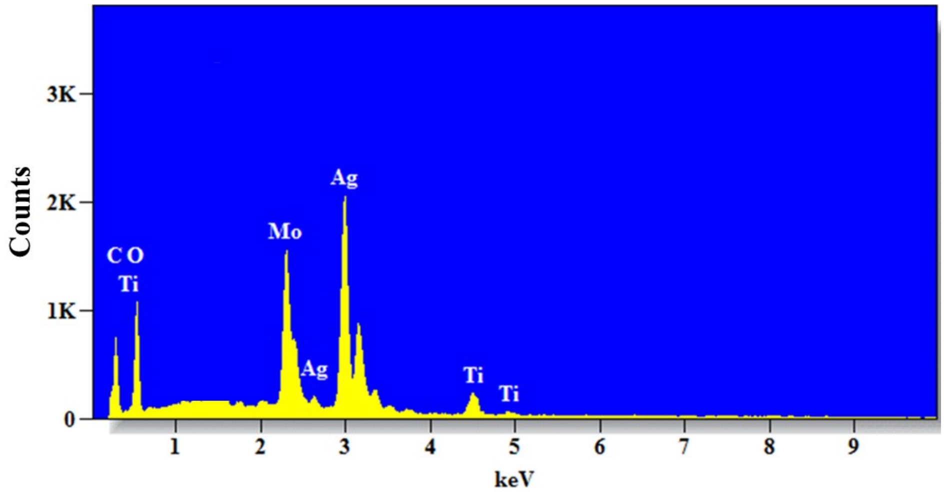

Figure S3. The EDX of M-TiO_2/β-Ag_2MoO_4-2 nanocomposite.

Table S1. Elemental composition of $Ti_3C_2T_x$, β-Ag_2MoO_4 and M-TiO_2/β-Ag_2MoO_4-2 nanocomposite.

Materials	Titanium	Silver	Molybdenum	Oxygen	Carbon	Fluorine
	at%	at%	at%	at%	at%	at%
$Ti_3C_2T_x$	53.0			6.0	16.0	25.5
β-Ag_2MoO_4		28.6	13.9	57.5		
M-TiO_2/β-Ag_2MoO_4-2	2.1	11.5	6.2	61.7	18.5	

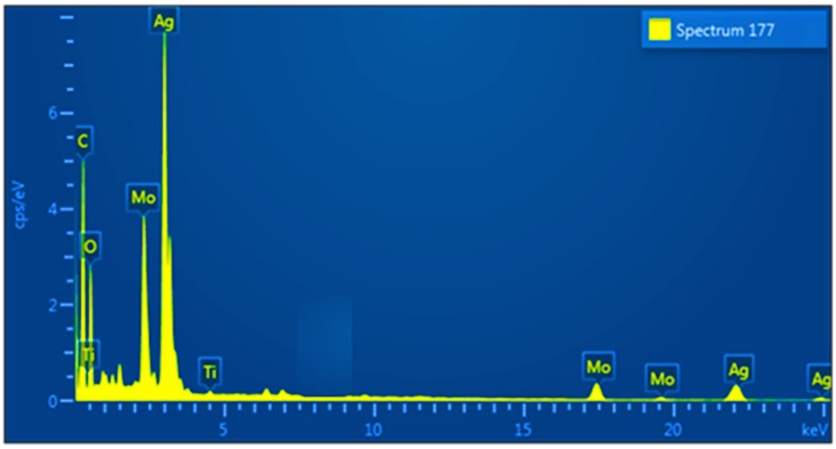

Figure S4. The EDS of M-TiO_2/β-Ag_2MoO_4-2 nanocomposite.

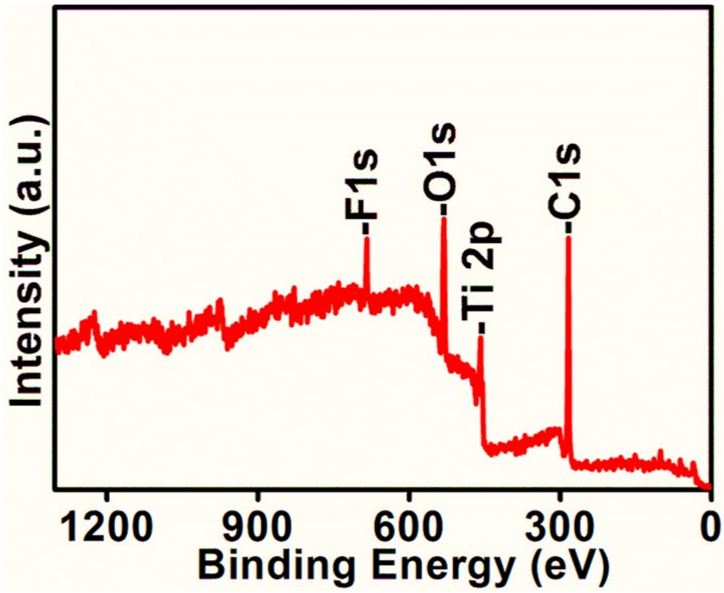

Figure S5. Survey spectrum of MXene ($Ti_3C_2T_x$).

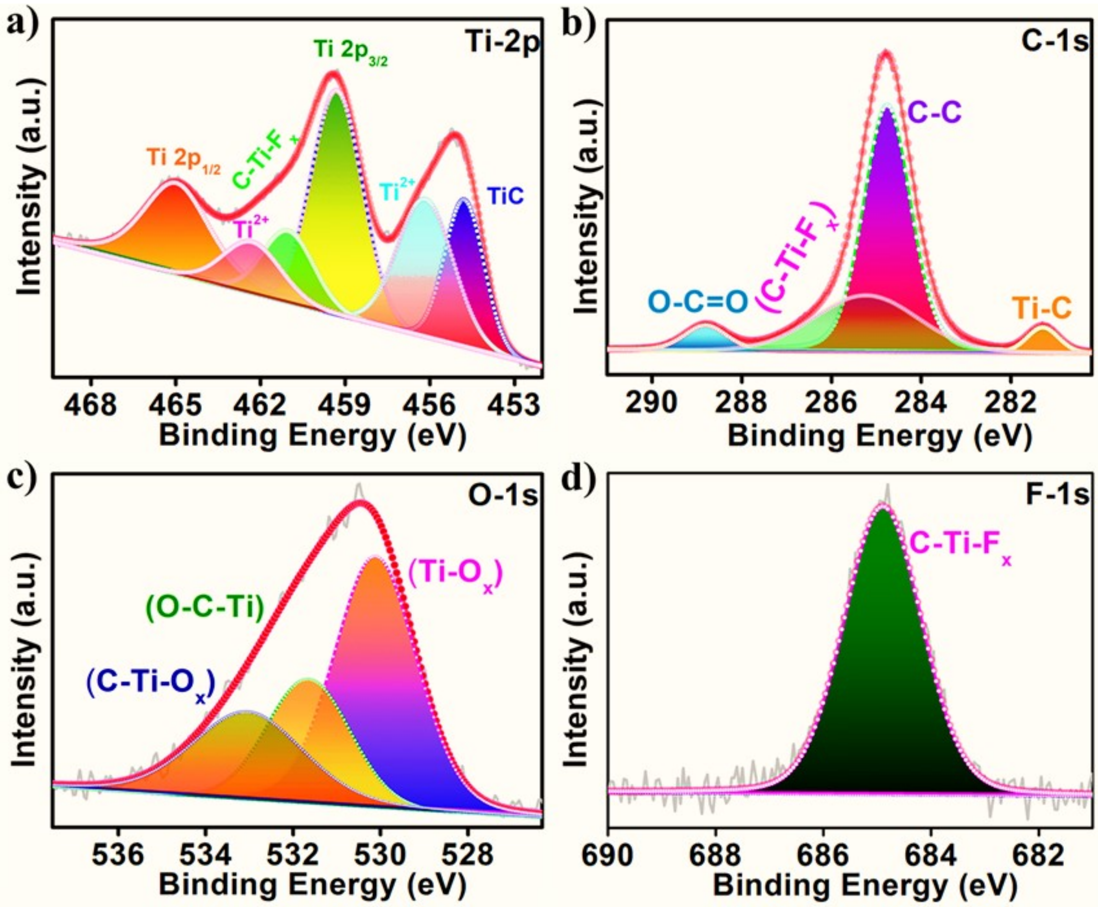

Figure S6. XPS of MXene ($Ti_3C_2T_x$); (a) Ti 2p, (b) C 1s, (c) O 1s, (d) F 1s.

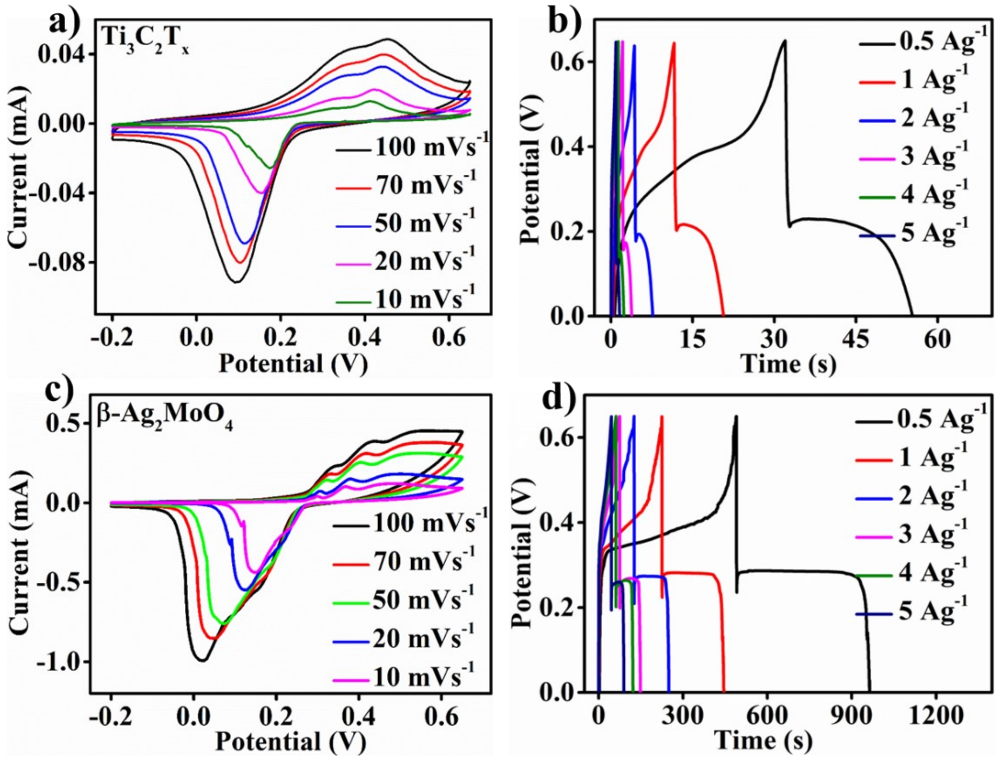

Figure S7. (a, c) CV curves at various scan rate and; (b, d) GCD profiles at different current density of $Ti_3C_2T_x$ and β-Ag_2MoO_4.

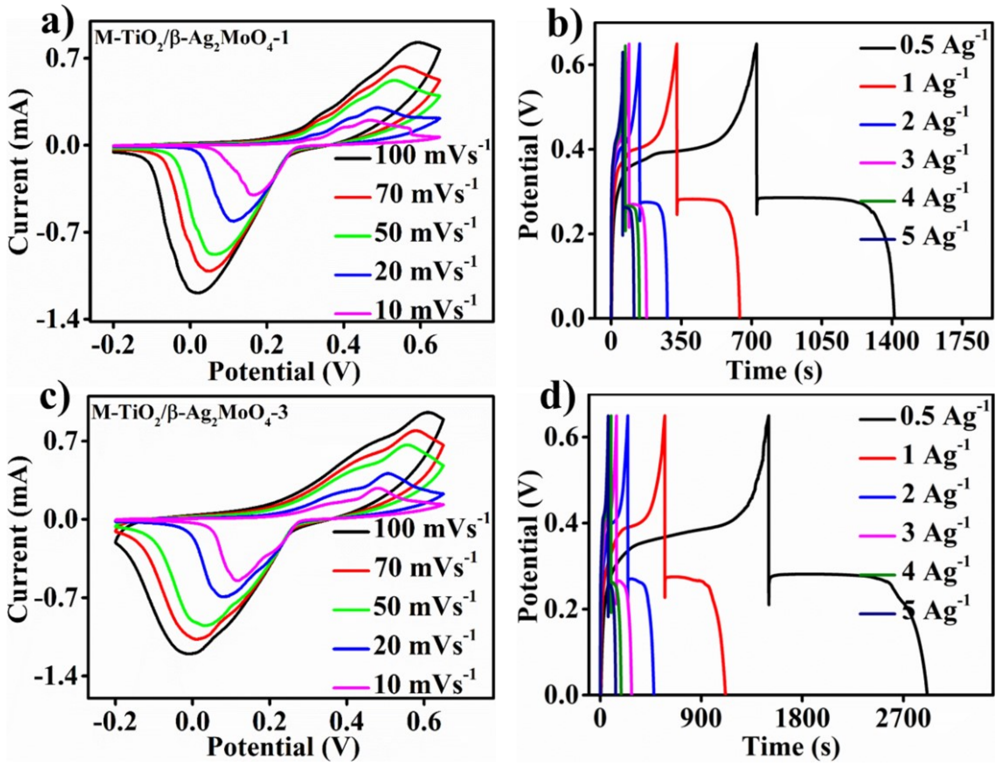

Figure S8. (a, c) CV curves at various scan rate and; (b, d) GCD profiles at different current density of M-TiO_2/β-Ag_2MoO_4-1 and M-TiO_2/β-Ag_2MoO_4-3 nanocomposite.

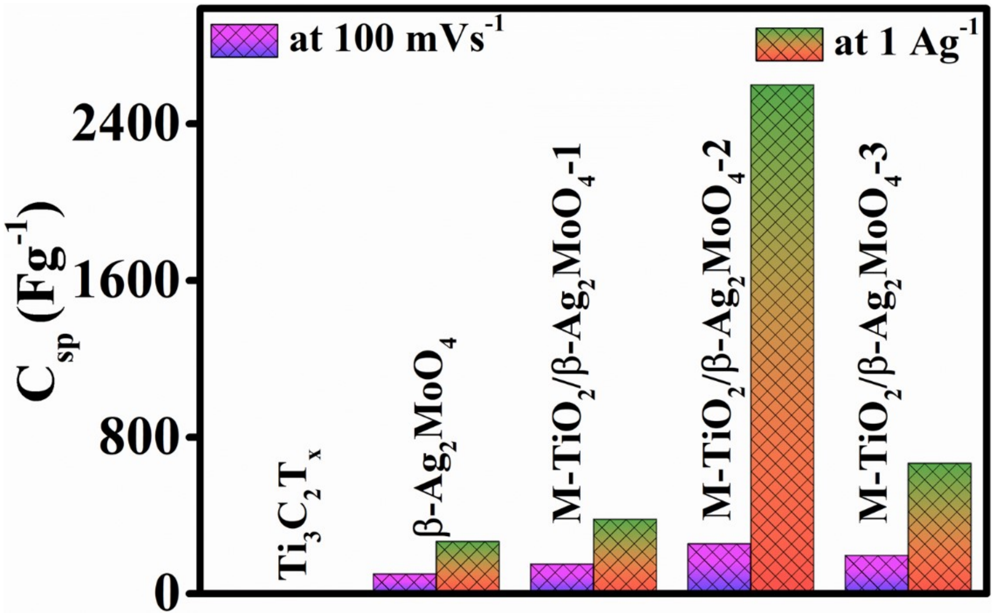

Figure S9. The calculated specific capacitance in three electrode configurations for various active electrode materials at 100 mV s^{-1} and 1 A g^{-1}.

Table S2. The calculated specific capacitance in three electrode configurations for various active electrode materials.

Materials	**Specific capacitance (F g^{-1})**	
	by CV @100 mV s^{-1}	**by GCD** @ 1 A g^{-1}
$Ti_3C_2T_x$	11.8	12.1
β-Ag_2MoO_4	100.8	266.6
M-TiO_2/β-Ag_2MoO_4-1	151.4	380.0
M-TiO_2/β-Ag_2MoO_4-2	255.8	2599
M-TiO_2/β-Ag_2MoO_4-3	195.4	666.2

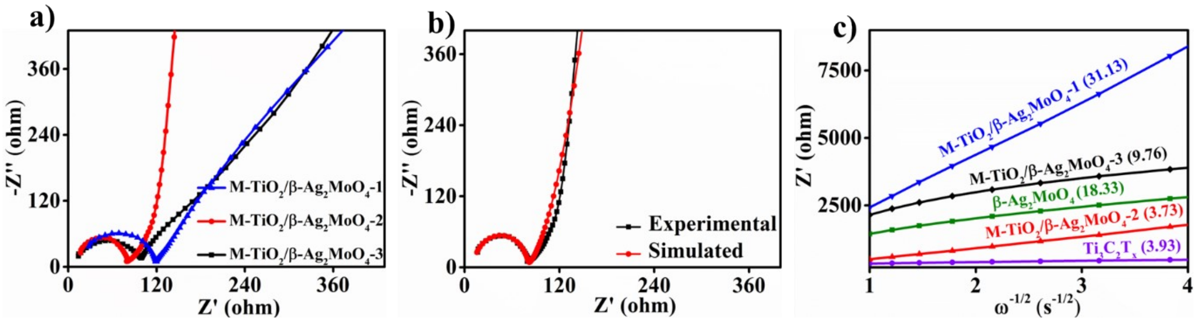

Figure S10. (a) Nyquist plots of all nanocomposites; (b) Experimental and fitted EIS curve for M-TiO_2/β-Ag_2MoO_4-2 electrode; (c) Plot of Z' versus reciprocal square root of frequency ($\omega^{-1/2}$).

Table S3. The transport properties of various electrodes were obtained from simulated impedance spectra in Fig. (5f)

Electrode	R_s (Ω)	R_{ct} (Ω)	σ = (Ω $s^{-1/2}$)	C_{ad} (mF)
$Ti_3C_2T_x$	14.4	113.8	3.93	5.6
β-Ag_2MoO_4	31.8	119.2	18.33	1.7
M-TiO_2/β-Ag_2MoO_4-1	28.1	116.8	31.13	0.07
M-TiO_2/β-Ag_2MoO_4-2	16.4	82.3	3.73	0.03
M-TiO_2/β-Ag_2MoO_4-3	13.8	99.1	9.76	0.05

Table S4. The calculated specific capacitance of M-TiO_2/β-Ag_2MoO_4-2 electrode material under the three-electrode configuration.

Cycles No.	Specific Capacitance (F g^{-1})	
	by CV @ 100 mV s^{-1}	**by GCD** @ 1 A g^{-1}
0k	255.8	2599
5k	198.5	2600
10k	208.7	2584
15k	209.8	2626
20k	204.7	2614
25k	195.5	2565

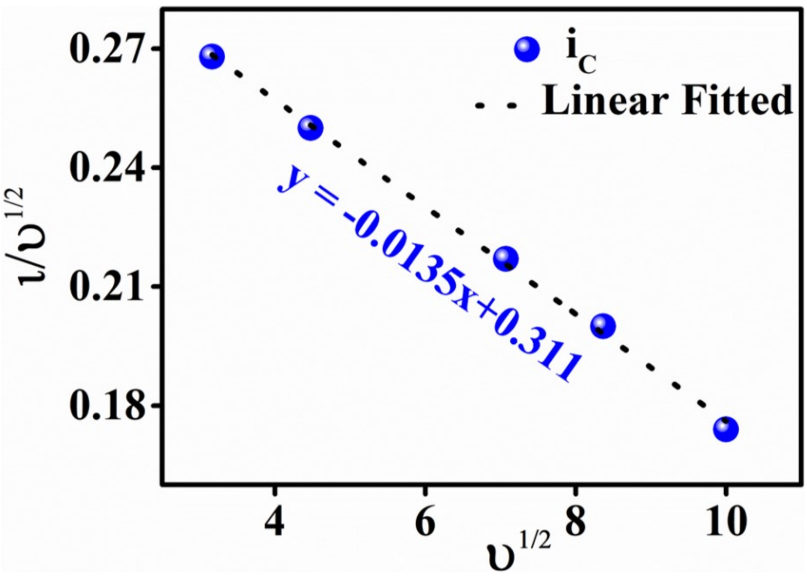

Figure S11. Plot of i/(scan rate, ν)$^{0.5}$ against $\nu^{0.5}$ for the cathodic sweeps under an alkaline medium to evaluate the value of k_1 and k_2 in the equation 12 and 13.

Table S5. The capacitive and diffusion contribution was calculated by the Dunn Method

v	$v^{1/2}$	**i**	k_1	k_2	k_1v	$k_2v^{1/2}$	$k_1v+k_2v^{1/2}$	$k_1v/i(v) = k_1v+k_2v^{1/2}*100$	$k_2v/i(v) = k_1v+k_2v^{1/2}*100-100$	**Toal capacity**	k_1v % (Fg^{-1})	$k_2v^{1/2}$ % (Fg^{-1})
10	3.162	0.86	0.0135	0.311	0.135	0.983382	1.118382	12.07100973	87.92899027	1218	146	1072
20	4.472	1.12	0.0135	0.311	0.27	1.390792	1.660792	16.25730374	83.74269626	811	130	681
50	7.071	1.54	0.0135	0.311	0.675	2.199081	2.874081	23.48576815	76.51423185	439	101	339
70	8.366	1.67	0.0135	0.311	0.945	2.601826	3.546826	26.64353989	73.35646011	343	92	251
100	10	1.74	0.0135	0.311	1.35	3.11	4.46	30.2690583	69.7309417	178	77	178

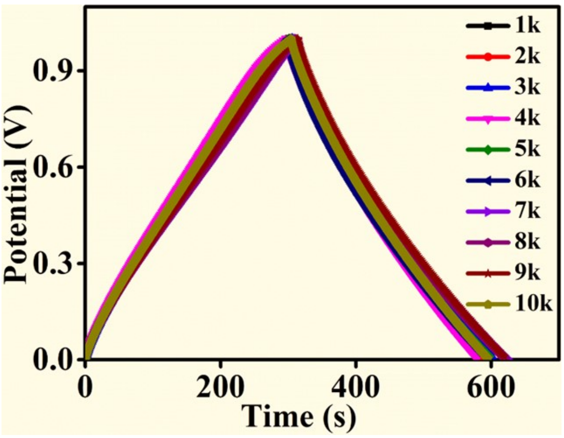

Figure S12. GCD curves at 1 A g^{-1} up to 10,000 cycles.

Table S6. The calculated specific capacitance on GCD curve of the as-fabricated symmetric coin cell supercapacitor throughout the stability performance.

Cycles No.	**Specific Capacitance (F g^{-1})** by GCD @ 1 A g^{-1}
1k	292.8
2k	285.0
3k	297.2
4k	283.4
5k	295.7
6k	290.2
7k	310.2
8k	309.0
9k	305.2
10k	290.4

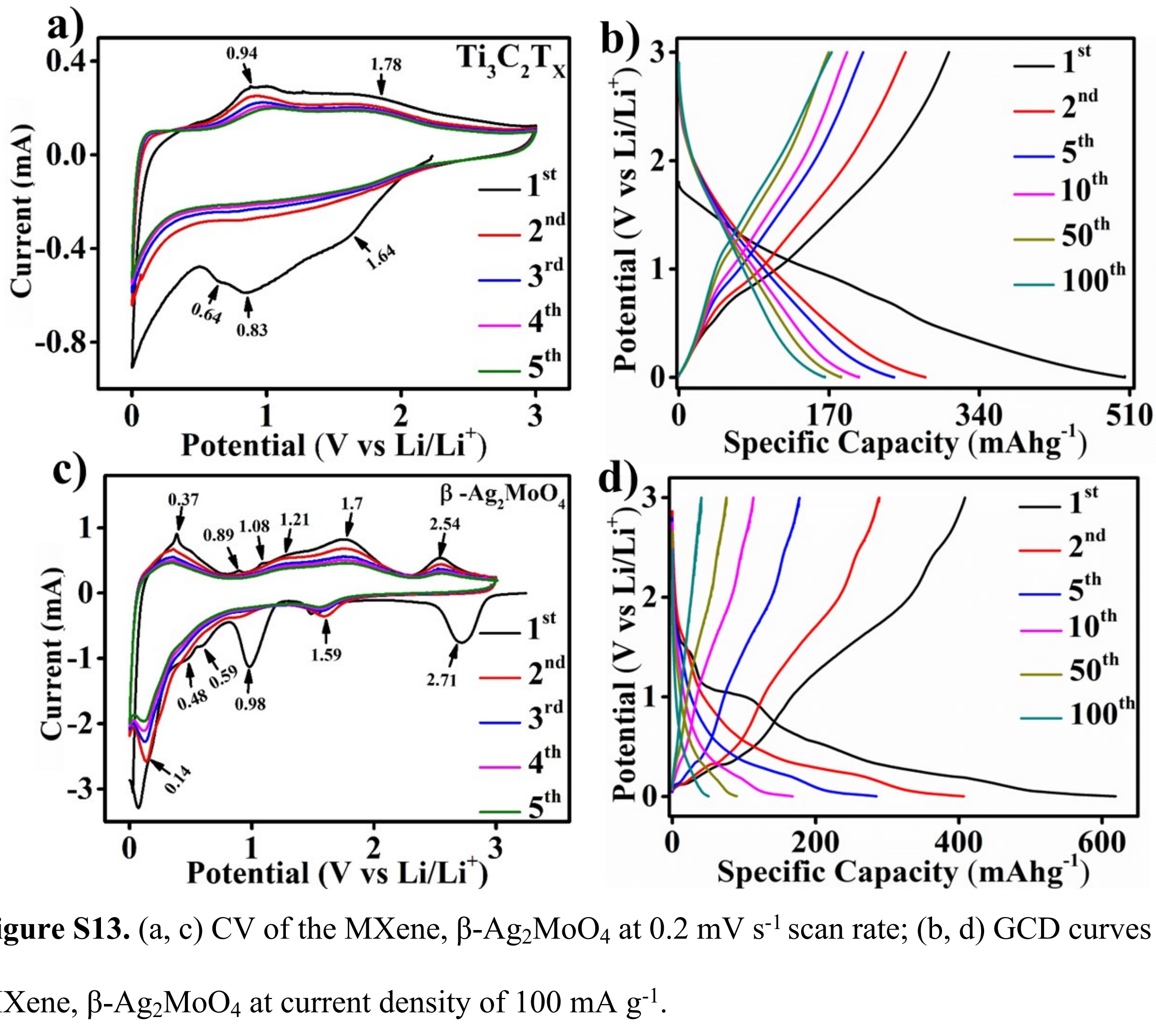

Figure S13. (a, c) CV of the MXene, β-Ag_2MoO_4 at 0.2 mV s^{-1} scan rate; (b, d) GCD curves of MXene, β-Ag_2MoO_4 at current density of 100 mA g^{-1}.

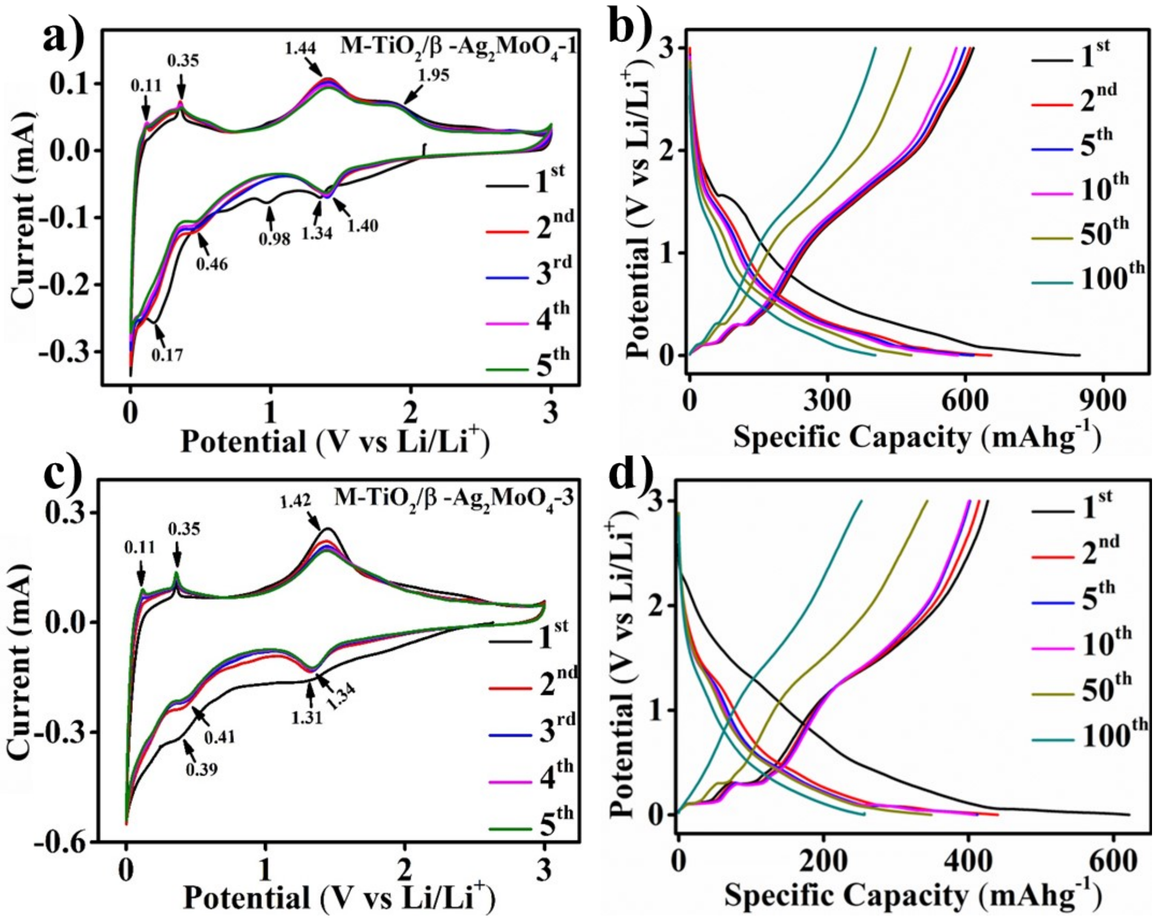

Figure S14. (a, c) CV of the M-TiO_2/β-Ag_2MoO_4-1 and M-TiO_2/β-Ag_2MoO_4-3 at 0.2 mV s^{-1} scan rate; (b, d) GCD curves of M-TiO_2/β-Ag_2MoO_4-1 and M-TiO_2/β-Ag_2MoO_4-3 at current density of 100 mA g^{-1}.

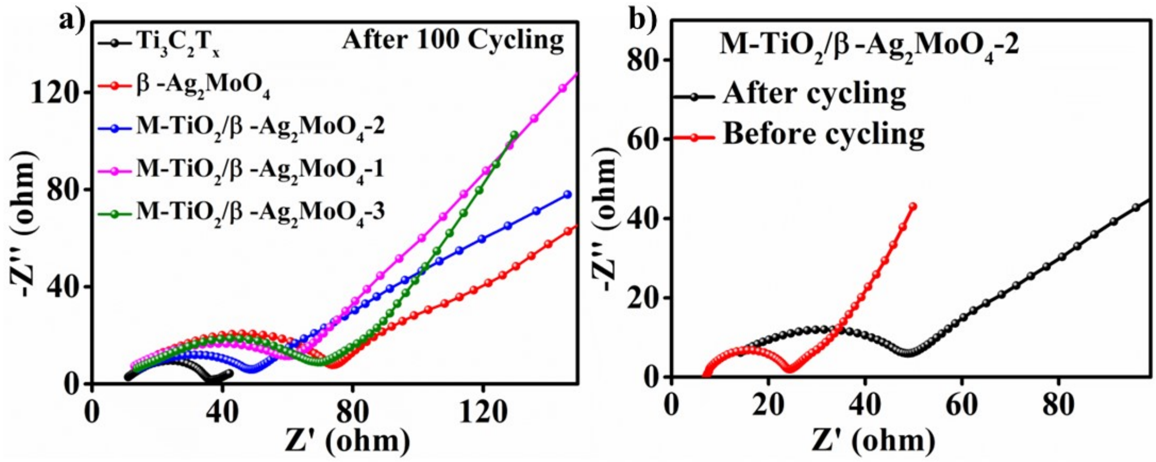

Figure S15. (a) EIS curve for MXene, β-Ag_2MoO_4 and all synthesized nanocomposites in the 0.1 Hz to 10 kHz frequency range. (b) Nyquist plot of after and before cycling stability of M-TiO_2/β-Ag_2MoO_4-2 nanocomposite.

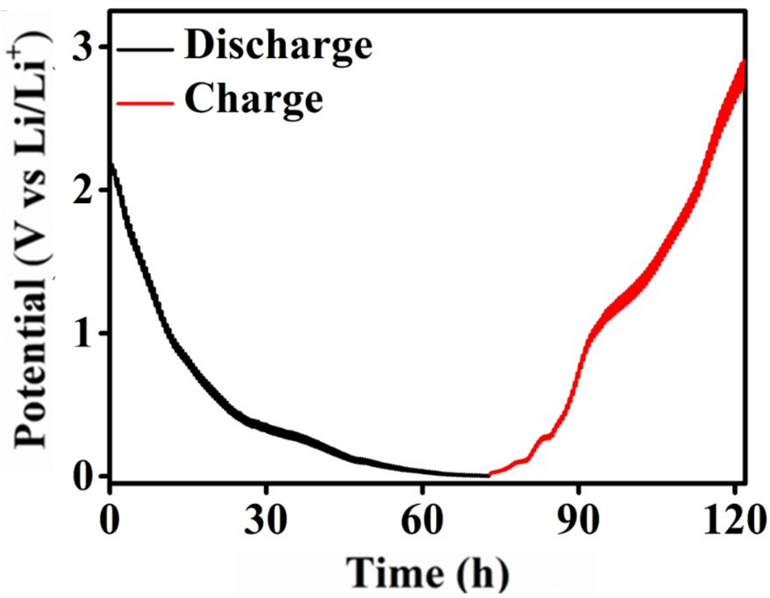

Figure S16. Galvanostatic intermittent titration technique (GITT) study of the M-TiO_2/β-Ag_2MoO_4-2 working electrode.

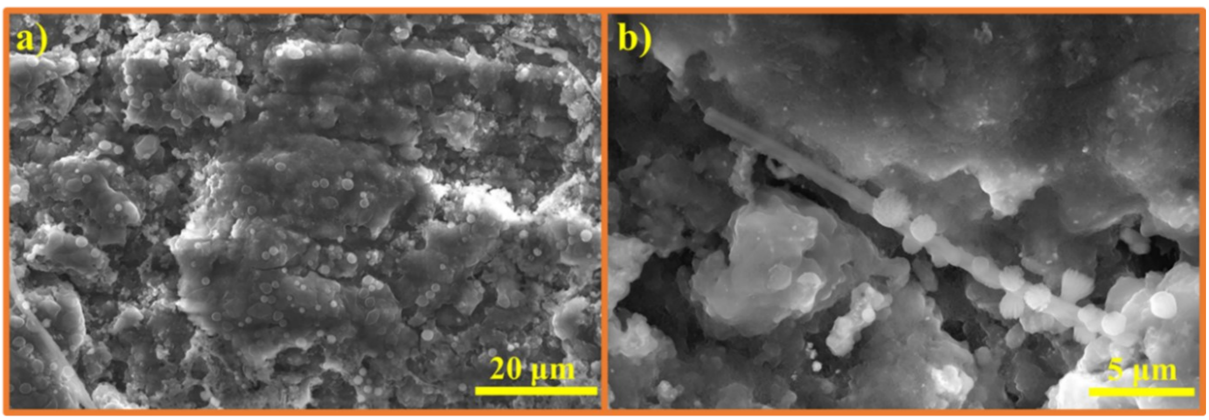

Figure S17. (a, b) HRSEM cross-section morphology of M-TiO_2/β-Ag_2MoO_4-2 working electrode after 100 cycles charge-discharge curve.

Table S7. The comparative electrochemical performance of the MXene and binary metal oxide-based electrode material for supercapacitor.

Materials	**Preparation Method**	**Electrolyte [Mol L^{-1}]**	**Specific Capacitance**		**Cycling Stability 3E (a)**	**Cycling Stability 2E (b)**	**Ref.**
			Electrode 3E (a)	**Device 2E (b)**			
$NiCo_2O_4$@ Fe_2O_3	Hydrothermal & Calcination	1.0 M Na_2SO_4	262 mF cm^{-2} at 1 mA cm^{-2}	----	74.2 % @4000	----	1

NiO/ $NiMoO_4$	Reflux & Calcination	6.0 M KOH	1624.5 F g^{-1} at 1.0 A g^{-1}	----	73.5 % @2200	----	2
$NiCo_2O_4$@ rGO/ACF	Hydrothermal & Calcination	3 M KOH	1338 mF cm^{-2} at 3 mA cm^{-2}	----	88.2 % @10 000	----	3
$NiMoO_4$/ $Ti_3C_2T_x$-10	Annealing	3 M KOH	483.8 C g^{-1} at 1.0 A g^{-1}	----	68.0 % @10 000	----	4
$NiZnCoO_4$/ $CoWO_4$-10	Hydrothermal & Calcination	2 M KOH	370.9 F g^{-1} at 0.5 A g^{-1}	----	90 % @500	----	5
$MnCo_2O_{4.5}$ @$NiCo_2O_4$	Hydrothermal & Calcination	3 M KOH	325 F g^{-1} at 1 A g^{-1}	----	70.5 % @ 3000	----	6
$ZnFe_2O_4$- rGO	Hydrothermal	2 M KOH	1419 F g^{-1} at 100 mV s^{-1}	101 F g^{-1} at 0.5 A g^{-1}	93 % @5000	90.1 % @5000	7
$Ti_3C_2T_x$/M nCo_2O_4	Hydrothermal & Calcination	1 M KOH	806.6 F g^{-1} at 1 A g^{-1}	----	77 % @3000	----	8
MoO_3/$Ti_3C_2T_x$	Hydrothermal	1 M KOH	151 F g^{-1} at 2 mV s^{-1}	----	93.7 % @8000	----	9
$Ti_3C_2T_x$/α- MoO_3	Hydrothermal	1 M Na_2SO_4	371 C g^{-1} at 1.0 A g^{-1}	----	89.5 % @6000	----	10
β- Ag_2MoO_4	Rapid wet chemical method	2 M KOH	2610 C g^{-1} at 1 A g^{-1}	----	82 % @5000	----	11
$Ti_3C_2T_x$/Ag_2CrO_4	co-precipitation method	0.1M H_2SO_4	525 F g^{-1} at 10 mV s^{-1}	----	----	----	12
$Ti_3C_2T_x$ /$CuCr_2O_4$	co-precipitation method	0.1M H_2SO_4	445.5 F g^{-1} at 20 mV s^{-1}	----	----	----	13
M-TiO_2/β-Ag_2MoO_4-2	**Reflux method**	**0.1 M KOH**	**2599 F g^{-1} at 1 A g^{-1}**	**309 F g^{-1} at 1 A g^{-1}**	**98.7 % @25000**	**95.1 % @10000**	**This Work**

Table S8. The comparative electrochemical performance of the MXene and binary metal oxide-based electrode material for Lithium-ion Battery.

Materials	Preparation Method	Initial discharge capacity (mA hg^{-1})	Capacity (mA hg^{-1})/ Cycles (times) @ current density mA g^{-1}	Ref.
C-Li_2MoO_4 nanotube	Sol-gel method	~ 650 mA hg^{-1}	~ 550 mA hg^{-1}/23@90 mA g^{-1}	14

MoO_3/C	Electro-spinning	1550 mA hg^{-1}	710 mA hg^{-1}/100 @40 mA g^{-1}	15
h-MoO_3	Reflux	1869 mA hg^{-1}	619 mA hg^{-1}/100@C/15	16
C-coated α-Na_2MoO_4 nanoplate	Sol-gel method	806 mA hg^{-1}	320 mA hg^{-1}/50@30 mA g^{-1}	17
MXene/Ag	Conventional method	550 mA hg^{-1}	310 mA hg^{-1}/800@1C	18
M-TiO_2/β-Ag_2MoO_4-2	**Reflux method**	**1013 mA hg^{-1}**	**335 mA hg^{-1}/100@100 mA g^{-1}**	**This work**

Table S9. The transport properties of various electrodes were obtained from impedance spectra in Fig S15.(a)

Electrode	**R_s(Ω)**	**R_{ct}(Ω)**
$Ti_3C_2T_x$	12.1	36.0
β-Ag_2MoO_4	20.6	73.5
M-TiO_2/β-Ag_2MoO_4-1	13.5	60.4
M-TiO_2/β-Ag_2MoO_4-2	15.1	47.9
M-TiO_2/β-Ag_2MoO_4-3	16.1	68.6

References

1 K. Zhang, Z. Cen, F. Yang and K. Xu, *Prog. Nat. Sci. Mater. Int.*, 2021, **31**, 19–24.

2 A. S. Keshari and P. Dubey, *Dalt. Trans.*, 2022, **51**, 3992–4009.

3 A. M. Patil, N. Kitiphatpiboon, X. An, X. Hao, S. Li, X. Hao, A. Abudula and G. Guan, *ACS Appl. Mater. Interfaces*, 2020, **12**, 52749–52762.

4 Y. Wang, J. Sun, X. Qian, Y. Zhang, L. Yu, R. Niu, H. Zhao and J. Zhu, *J. Power Sources*, 2019, **414**, 540–546.

5 R. R. Neiber, J. Kumar, R. A. Soomro, S. Karkus, H. M. Abo-Dief, A. K. Alanazi, A. A. Altalhia and Z. M. El-Bahy, *J. Energy Storage*, 2022, **52,** 104900.

6 W. C. Huo, X. L. Liu, Y. S. Yuan, N. Li, T. Lan, X. Y. Liu and Y. X. Zhang, *Front. Chem.*, 2019, **7**, 1–9.

7 M. B. Askari, P. Salarizadeh, M. Seifi, M. H. Ramezan zadeh and A. Di Bartolomeo, *J. Alloys Compd.*, 2021, **860**, 158497.

8 Q. Xia, W. Cao, F. Xu, Y. Liu, W. Zhao, N. Chen and G. Du, *J. Energy Storage*, 2022, **47**, 103906.

9 J. Zhu, X. Lu and L. Wang, *RSC Adv.*, 2016, **6**, 98506–98513.

10 Z. Pan, C. Yang, Y. Li, X. Hu and X. Ji, *Chem. Eng. J.*, 2022, **428,** 131138.

11 J. J. William, S. Balakrishnan, M. Murugesan, M. Gopalan, A. J. Britten and M. Mkandawire, *Mater. Adv.*, 2022, **3**, 8288–8297.

12 T. Yaqoob, M. Rani, A. Mahmood, R. Shafique, S. Khan, N. K. Janjua, A. A. Shah, A. Ahmad and A. A. Al-Kahtani, Materials, 2021, **14**, 6008.

13 R. Shafique, M. Rani, K. Batool, A. A. Alothman, M. S. Saleh Mushab, A. A. Shah, A. Kanwal, S. Ali and M. Arshad, *J. Mater. Res. Technol.*, 2023, **24**, 2668–2677.

14 X. Liu, Y. Lyu, Z. Zhang, H. Li, Y. S. Hu, Z. Wang, Y. Zhao, Q. Kuang, Y. Dong, Z. Liang, Q. Fan and L. Chen, *Nanoscale*, 2014, **6**, 13660–13667.

15 C. Feng, H. Gao, C. Zhang, Z. Guo and H. Liu, *Electrochim. Acta*, 2013, **93**, 101–106.

16 Udayabhanu, V. Pavitra, M. Shivanna, F. A. Alharthi, B. M. Praveen, Y. T. Ravikiran, K. Byrappa and G. Nagaraju, *Int. J. Energy Res.*, 2021, **45**, 17315–17326.

17 X. Liu, Y. Zhao, Y. Dong, Q. Kuang, Z. Liang, X. Lin, D. Yan and H. Liu, *Electrochim. Acta*, 2015, **154**, 94–101.

18 G. Zou, Z. Zhang, J. Guo, B. Liu, Q. Zhang, C. Fernandez and Q. Peng, *ACS Appl. Mater. Interfaces*, 2016, **8**, 22280–22286.